Journal of Engineering Mathematics **45:** 91–104, 2003.

The role of hemodynamics in the development of the outflow tract of the heart

ERWIN LOOTS[1], BEREND HILLEN[2] and ARTHUR E.P.VELDMAN[1]
[1]*Department of Mathematics, University of Groningen, P.O. Box 800, 9700 AV Groningen, The Netherlands (e-mail: g.e.loots@math.rug.nl)*
[2]*Department of Anatomy, Universal Medical Centre, University of Nijmegen, P.O. Box 9101, 6500 MB Nijmegen, The Netherlands (e-mail: b.hillen@anat.kun.nl)*

Received 26 September 2002; accepted in revised form 30 September 2002

Abstract. The question whether, and if so to what extent, hemodynamic forces and mechanical stimuli do modulate the morphogenesis of the vascular system is a century-old problem. It is important especially in the outflow tract where a spiraling septum develops in and after a strong bend in the tube. Spiraling patterns of the flow in bends are well known. Of the mechanical stimuli that can potentially exert an effect on morphogenesis, wall shear stress is the most likely candidate; a number of genes that are expressed in the cardiovascular system have shear-stress responsive elements in their regulatory units. Recent investigations have clearly shown that the disturbance of normal hemodynamic conditions results in maldevelopment of the heart. However, an experimental model alone is necessary, but not sufficient to identify the intermediate steps of the interaction between blood flow and tissue remodeling in the developing cardiovascular system, certainly at Reynolds numbers and Dean numbers that are very small. Therefore, a model with a simple geometry has been created, using the ComFlo software: a fully 3D computational fluid-dynamics code that solves the Navier-Stokes equations on a Cartesian grid. A first assessment of the possible influence of a strong curvature, with biological realistic dimensions, was made using steady-flow conditions. Since both the Reynolds number and the Womersley number (indicating the influence of the pulsatility on the velocity profile of the flow) are extremely low, it is likely that these flow patterns do not differ significantly from those under pulsatile conditions. A first assessment of the effects of the strong curvature on the flow under the given circumstances showed only very small secondary velocities and negligible heterogeneity of the wall shear stress, even in the presence of a strong secondary flow pattern in the inlet of the tube.

Key words: Cartesian grid, hemodynamics, wall shear stress

1. Introduction

Congenital heart defects account for the largest component of infant mortality. The question whether and if so, to what extent hemodynamic forces and mechanical stimuli do modulate the morphogenesis of the vascular system is a century-old problem. Recently, it was demonstrated [1] that manipulating the blood flow in the embryo results in malformations and suggests that this is the result of altered flow patterns and consequently altered hemodynamic forces. The mechanical stimulus that is most likely to exert an effect on morphogenesis is the wall shear stress (WSS, the friction between vessel wall and blood flow). A number of genes that are expressed in the cardiovascular system, have shear-stress responsive elements in their regulatory units [2–4]. However, WSS is an elusive parameter that cannot be measured directly. In order to associate gene expression with hemodynamic forces, mathematical modeling of shape and flow is a prerequisite. In a first assessment we focus on the spiraling septation of the outflow tract in the developing heart that has been associated with helical flow patterns.

In the early stages of development the heart is a single tube with a very strong bend. Flow patterns in curved tubes were first studied by Dean in 1927 [5]. In his paper he describes the double helical flow pattern and introduces a dimensionless parameter based on the Reynolds number and the ratio of the tube diameter and the radius of the curvature, later known as the Dean number, to relate the strength of the secondary flow field and the geometry of the tube. Since then the flow in curved tubes has been studied by various authors, both mathematically [6–13] and experimentally [14, 15]. From these publications it can be extrapolated that at the estimated Dean and Reynolds numbers in the developing heart, the influence of the geometry on the flow pattern will be minimal. Estimates of the Reynolds number range from 0·4 to 40 in the development of the heart; since the ratio of the diameter of the tube and its radius of curvature is close to 1, the Dean numbers have approximately the same values. To the best of our knowledge, there have been neither studies focusing on the heterogeneity of the shear-stress distribution in bends of such a small size, nor on the attenuation of secondary flows in the entry of the tube.

From embryological studies in the chick, two interesting observations were made. Firstly, in 1932 Bremer [16] traced two masses of blood cells in a motion-picture film of the living heart of a 48 hrs chick embryo (Figure 1) and noted a rotation of the flow in the atrial cavity (the part of the tube where the blood enters the heart tube) and assumed it to continue in the outflow tract. Secondly, in 1987 Seidl and Sterling [17] visualized streamlines using injections with Evans Blue an noted a rotation of the flow in the outflow tract in a 72 hrs chick embryo and subsequent stages and concluded that the changing morphology precedes and induces the spiraling flow rather than the other way around.

Our first step in assessing the hemodynamic phenomena that may be involved in the development of the outflow tract is to create a mathematical model with a simplified geometry. A specific feature of ComFlo is that it covers the domain with a Cartesian grid and uses the cut-cell approach at the boundaries, while most available software packages apply boundary-fitted meshes instead. Especially in combination with free surfaces and (visco-)elastic boundaries this approach is quite useful.

The geometry (Figure 4) closely resembles the 48 hrs stage as presented by Bremer (Figure 1). With this model flow patterns and WSS distribution were investigated using various boundary conditions; pulsatility is ignored and the Reynolds number is equal to unity. Effects of higher Reynolds numbers are also investigated.

The remainder of the paper is structured as follows: in Section 2, the main features of our computational model are explained, with extra emphasis on the finite-volume approach and the computation of the wall shear stress. Then, in the Results section, the numerical set-up is discussed and the influence of a secondary-flow pattern in the inlet part of the tube studied. After that, we investigate the influence of the bend on the generation of a secondary velocity field in the outlet part. Finally, in Section 4 these results are discussed.

2. The model

2.1. The fluid equations

Because we are considering vessels with diameters that have a far larger scale than the microstructures in blood, the fluid can be considered a homogeneous Newtonian fluid. Therefore, the incompressible Navier-Stokes equations are used:

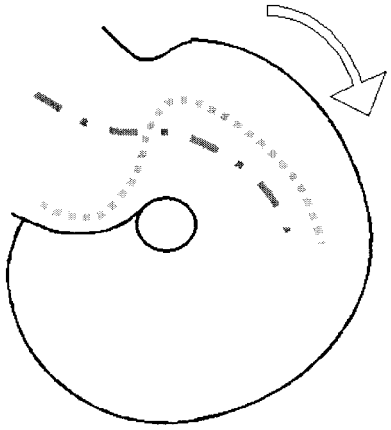

Figure 1. Diagram of the tracings of two blood-cell masses in the inlet of the developing heart tube of a chick embryo of 48 hrs. (redrawn from the original publication of Bremer) The arrow indicates the flow direction.

conservation of mass

$$\int_{\partial V} \boldsymbol{u} \cdot \boldsymbol{n} \, \mathrm{d}S = 0, \tag{1}$$

conservation of momentum

$$\int_{V} \frac{\partial \boldsymbol{u}}{\partial t} \mathrm{d}V + \int_{\partial V} \boldsymbol{u}\boldsymbol{u}^T \cdot \boldsymbol{n} \, \mathrm{d}S = -\frac{1}{\rho} \int_{\partial V} (p\boldsymbol{I}_3 - \mu \nabla \boldsymbol{u}) \cdot \boldsymbol{n} \, \mathrm{d}S. \tag{2}$$

where $\boldsymbol{n}$ is the normal on the boundary of the control volume V and $\boldsymbol{I}_3$ is the 3×3 identity matrix.

The formulation above is written in the so-called conservation form and is called the weak formulation of the Navier-Stokes equations. This formulation is the basis of the finite-volume method.

There are several ways to model inflow and outflow boundary conditions in tube-like geometries. The most standard combination is to prescribe the velocity in the inflow area: $\boldsymbol{u} = \boldsymbol{u}_{\text{in}}$ and to set a homogeneous Neumann condition at the outlet: $\partial \boldsymbol{u}/\partial \boldsymbol{n} = 0$ combined with a reference pressure $p = p_{\text{out}}$.

We choose the inflow velocity $\boldsymbol{u}_{\text{in}}$ such that we get Poiseuille flow: $u = U(1 - r^2/R^2)$, $v = w = 0$ and $\text{Re} = UR/\nu$. It is also possible to prescribe secondary velocities v and w in the inflow area (see Section 3.2).

2.2. DISCRETIZATION

Many CFD codes have in common that they use body-fitted coordinates. Although this has advantages in the field of boundary treatment, the construction of new grids for each separate problem is often more costly than the simulation itself. Our approach is to use a finite-volume discretization of the Navier-Stokes equations on a simple, rectilinear (Cartesian) grid, thus enabling applications with arbitrary complex (3D) geometries. The drawback of this are the measures that have to be made at the non-gridaligned boundaries; here we make use of the so-called cut-cell approach [18, 19].

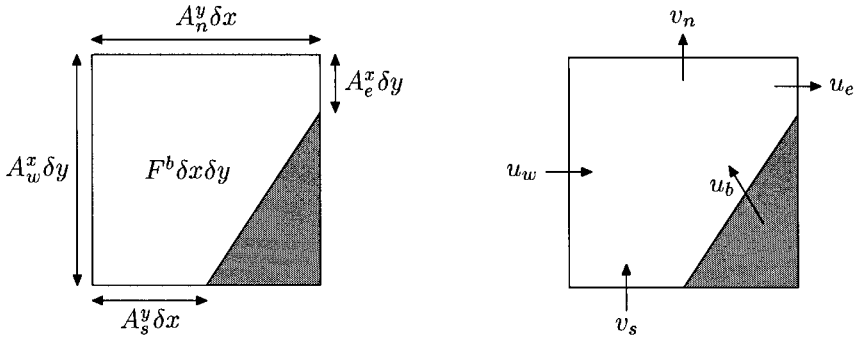

Figure 2. Illustration of the volume and edge apertures (left) and the location of the velocities (right). The shaded area represents solid body.

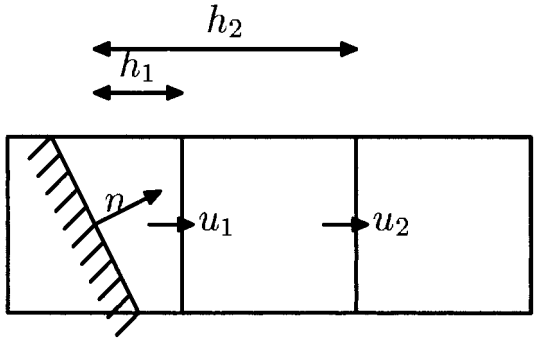

Figure 3. Computation of $\frac{\partial u}{\partial x}$.

While the code was originally intended for free-surface computations (using Eulerian VOF-functions and local level set methods, [20]), modeling of elastic walls has recently been implemented.

Since our computational domain should be able to change continuously (*i.e.*, the boundaries might move) and we do not want to re-mesh again and again, we take the simple approach to cover the smallest bounding box of the time-dependent domain with a rectilinear grid. Then the boundaries will, in general, not coincide with the grid lines: the cells are (possibly time-dependently) cut. This leads to the introduction of *apertures*: scalars in which all the geometry information is contained. There are two variants: cell apertures and edge apertures. A cell aperture $F_b (0 \leq F_b \leq 1)$ denotes the fraction of the cell that is occupied by fluid; an edge aperture A_x, A_y or A_z denotes the fraction of a cell face where the fluid is able to flow between the two cells which share that cell face (see also Figure 2).

Inside the computational domain the fluid equations have to be solved. These are the incompressible Navier-Stokes equations as described above. Following the MAC-method, the velocities are placed at the cell faces and the pressure at the cell centres. Discretization of the convective and diffusive terms is done by taking the apertures into account, thereby using the finite-volume method. The coefficient matrix for convection is skew-symmetric and the matrix for diffusion symmetric and positive definite, leading to a stable numerical method [21]. The system is solved using the pressure-correction method.

We will show, in 2D, the finite-volume discretization of the equation describing mass conservation (Equation 1). Consider the standard case of a computational cell which is partly cut

by the solid boundary, as shown in the right part of Figure 2. Following the MAC-method, the velocities are staggered, meaning that horizontal velocities u_w and u_e are placed at vertical cell faces and vertical velocities like v_s and v_n are placed on horizontal cell faces. The mentioned velocities hold along the entire open part of their cell faces; this means that the velocity arrows could also have been drawn at any other position on the open parts of the cell faces where they are positioned. The control volume V for the discretization of the equation is the open part of the computational cell. Discrete conservation of mass means that the sum of all mass fluxes $(\rho \boldsymbol{u}) \cdot \boldsymbol{n}$ through the boundary ∂V is zero. We split ∂V in the integral into five straight pieces; applying the midpoint rule for each of these smaller integrals causes no errors, since the velocities are piecewise constant. For our cell in Figure 2 this gives

$$-A_w^x \delta y u_w + A_n^y \delta x v_n - A_s^y \delta x v_s + A_e^x \delta y u_e + u_b l = 0, \tag{3}$$

where $l = \sqrt{((1 - A_s^y)\delta x)^2 + ((1 - A_e^x)\delta y)^2}$ is the length of the solid boundary in the cell. The last term of the left-hand side is the mass flux through this solid boundary and is zero in our application (alternatively, one can interpret u_b to be the velocity of a moving interface, and, using the compressible variant of (1), one can derive an equation for moving walls similar to Equation 3). For a computational cell in the interior, that is, when the cell does not contain a part of the solid boundary, all the edge apertures are equal to one and Equation (3) reduces to a second-order central discretization of the continuity equation $\nabla \cdot \boldsymbol{u} = 0$ (which, in turn, results from applying Gauss's theorem to Equation (1):

$$\frac{u_w - u_e}{\delta x} + \frac{v_n - v_s}{\delta y} = 0.$$

2.3. WALL SHEAR STRESS

The deformation tensor, or shear of rate tensor is of the form:

$$E = \frac{1}{2} \begin{pmatrix} 2\dfrac{\partial u}{\partial x} & \dfrac{\partial u}{\partial y} + \dfrac{\partial v}{\partial x} & \dfrac{\partial u}{\partial z} + \dfrac{\partial w}{\partial x} \\ \dfrac{\partial u}{\partial y} + \dfrac{\partial v}{\partial x} & 2\dfrac{\partial v}{\partial y} & \dfrac{\partial v}{\partial z} + \dfrac{\partial w}{\partial y} \\ \dfrac{\partial u}{\partial z} + \dfrac{\partial w}{\partial x} & \dfrac{\partial v}{\partial z} + \dfrac{\partial w}{\partial y} & 2\dfrac{\partial w}{\partial z} \end{pmatrix}. \tag{4}$$

A very important quantity is the scalar derived from this sensor at the wall, called wall shear stress (WSS) or shear rate. More precisely, the WSS is the frictional force the fluid exerts on the material. The WSS has a nonnegative value independent of direction. Alternatively, it is defined as $\mu |\partial \boldsymbol{u} / \partial \boldsymbol{n}|$ where $\boldsymbol{n}$ is the normal at the wall and μ the dynamic viscosity. In a tube having radius R, with Poiseuille flow $u(r) = U(1 - r^2/R^2)$ and $v = w = 0$, the derivative at the wall is $\partial u / \partial r|_{r=R} = -2U/R$ and the WSS therefore reduces to $\mu 2U/R$. To obtain the WSS using only the standard derivatives in x-, y- and z-directions, we start with

$$\frac{\partial u}{\partial x} = \frac{\partial u}{\partial \boldsymbol{n}} n_x + \frac{\partial u}{\partial \boldsymbol{t}} t_x = \frac{\partial u}{\partial \boldsymbol{n}} n_x,$$

where $\boldsymbol{n}$ and $\boldsymbol{t}$ are the normal and tangential direction vectors, respectively. Furthermore, $n_x = \boldsymbol{n} \cdot \boldsymbol{e_1}$ and thus $\boldsymbol{n} = (n_x, n_y, n_z)^T$. The second equality holds since $\partial u / \partial \boldsymbol{t} = 0$ can be assumed.

And therefore, since the same applies to derivatives in y- and z-directions, we have

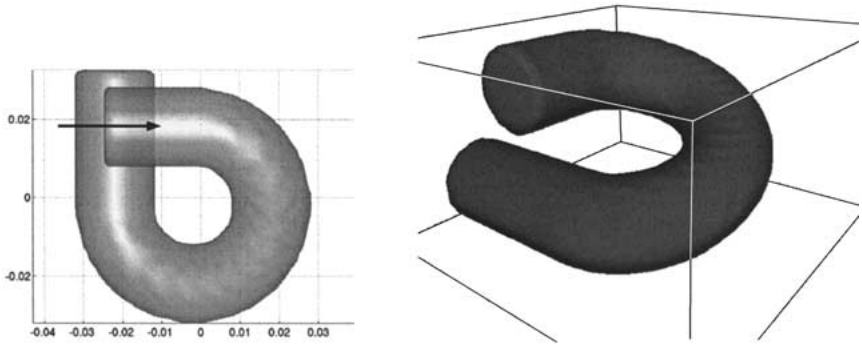

Figure 4. Left picture: top view of the model geometry; right picture: bird-eye view.

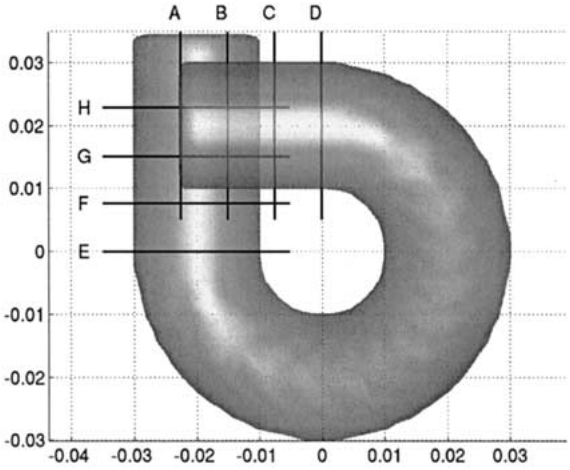

Figure 5. Overview of the positions of the velocity plots.

$$\frac{\partial u}{\partial \boldsymbol{n}} = \frac{1}{n_x}\frac{\partial u}{\partial x} = \frac{1}{n_y}\frac{\partial u}{\partial y} = \frac{1}{n_z}\frac{\partial u}{\partial z}. \tag{5}$$

An indication of the magnitude of the WSS is obtained by using the Euclidean norm $|(\frac{\partial u}{\partial \boldsymbol{n}}, \frac{\partial v}{\partial \boldsymbol{n}}, \frac{\partial w}{\partial \boldsymbol{n}})^T|$ of the velocity derivatives in the normal direction. So, in principle, each of the three expressions (5) can be used to compute $\partial u/\partial \boldsymbol{n}$. Because of the numerical errors and difficulties (the discrete location of the velocities and the determination of the distances), these three values can differ considerably. Therefore, a weighted average is used: $\frac{\partial u}{\partial \boldsymbol{n}} = w_1 \frac{1}{n_x}\frac{\partial u}{\partial x} + w_2 \frac{1}{n_y}\frac{\partial u}{\partial y} + w_3 \frac{1}{n_z}\frac{\partial u}{\partial z}$ and we choose for the weight factors the squares of the components of the normal vector at the wall: $w_1 = (n_x)^2$, etc:

$$\frac{\partial u}{\partial \boldsymbol{n}} = n_x \frac{\partial u}{\partial x} + n_y \frac{\partial u}{\partial y} + n_z \frac{\partial u}{\partial z}; \tag{6}$$

note that the sum of the weight factors is exactly $|\boldsymbol{n}| = 1$. Interestingly, the result is the same as the analytical definition $\frac{\partial u}{\partial \boldsymbol{n}} = \boldsymbol{n} \cdot \nabla u$. Note further that $(\frac{\partial u}{\partial \boldsymbol{n}}, \frac{\partial v}{\partial \boldsymbol{n}}, \frac{\partial w}{\partial \boldsymbol{n}})^T = E \cdot \boldsymbol{n} - \nabla(\boldsymbol{u} \cdot \boldsymbol{n})$.

Since the WSS is a function of the derivative of velocities, it is rather sensitive to perturbations. Therefore, besides a good determination of the normal, a good approximation of the distance from the wall is needed. To compute the derivatives, the two nearest momentum velocities near the wall are taken. Here we use the notion of velocity components on the

standard MAC-locations (velocity $u(i)$ placed in the centre of the edge between cells i and $i+1$, etc.) and disregard the finite-volume approach (where the same value of a velocity holds in its entire control volume) for the moment. Together with the wall velocity u_w this gives three velocities u_w, u_1, u_2 and three distances $0, h_1, h_2$. Fitting a parabola through these points we have

$$u_1 = ah_1^2 + bh_1 + u_w, \quad u_2 = ah_2^2 + bh_2 + u_w;$$

thus

$$a = \frac{h_2u_1 - h_1u_2 - u_w(h_2 - h_1)}{h_1^2h_2 - h_1h_2^2}; \quad b = \frac{u_2 - u_w}{h_1} - ah_1 \tag{7}$$

and $\lim_{h\to 0} \frac{\partial u}{\partial x} = 2ah + b|_{h=0} = b$. This computation is valid, *i.e.*, b and a are bounded, if $h_2 > h_1 > 0$. The first inequality holds because of the construction of h_1 and h_2: $h_2 = h_1 + h_x$, where h_x is the width of the cell between the locations of the velocities u_1 and u_2. The second inequality is fulfilled when u_1 is not a mirror (boundary) velocity but represents a physical flux. When $h_1 < \epsilon$, the velocities u_1 and u_2 are shifted in the direction of the interior (that is, u_1 becomes the old u_2 and u_2 is then located one cell further from the wall). The distances h_1 and h_2 are computed using the geometry apertures F_b (see Figure 3). This computation is less accurate when the direction is more or less aligned with the tangent of the wall; fortunately, in that case the weight of the term in the computation of $\partial u/\partial \boldsymbol{n}$ (Equation (6)) is small.

We compare normals using the apertures, which are the only quantities that contain the geometrical information. For the computation of $\partial u/\partial \boldsymbol{n}$, the non-normalized normal is given by (note that the velocity u_i is located on the cell face between cell i and $i+1$):

$$\begin{aligned} n_x = \frac{1}{h_x}(&F_b^{i+1,j,k} + F_b^{i+1,j-1,k} + F_b^{i+1,j+1,k} + F_b^{i+1,j,k-1} + F_b^{i,j,k+1} - \\ &F_b^{i,j,k} - F_b^{i,j-1,k} - F_b^{i,j+1,k} - F_b^{i,j,k-1} - F_b^{i,j,k+1}), \end{aligned}$$

$$n_y = \frac{1}{h_y}(A_x^{i,j+1,k} + A_x^{i,j+1,k+1} + A_x^{i,j+1,k+1} + A_x^{i,j-1,k} - A_x^{i,j-1,k+1} - A_x^{i,j-1,k-1}),$$

$$n_z = \frac{1}{h_z}(A_x^{i,j,k+1} + A_x^{i,j,k+1} + A_x^{i,j-1,k+1} - A_x^{i,j,k-1} - A_x^{i,j,k-1} - A_x^{i,j-1,k-1}).$$

3. Numerical results

3.1. SET-UP

The model geometry is shown in Figure 4. It consists of a helix with straight cylindrical parts at the beginning (upper left) and at the end (lower left). The radius of the helix is $r = 0{\cdot}01$ m, the radius of curvature of the central axis $R = 0{\cdot}02$ m. Therefore the Dean number D is $r/R = 1/2$. The dimensions of the computational domain are: $-0{\cdot}04 < x, y < 0{\cdot}04$; $-0{\cdot}022 < z < 0{\cdot}022$. The straight inflow part is defined for $0{\cdot}002 < z < 0{\cdot}022$; the straight outflow part is bounded by $-0{\cdot}022 < z < -0{\cdot}002$. Therefore, the height of the central axis decreases from $z = 0{\cdot}012$ to $z = -0{\cdot}012$. To ensure sufficient smoothness, this decrease is not linear but follows from

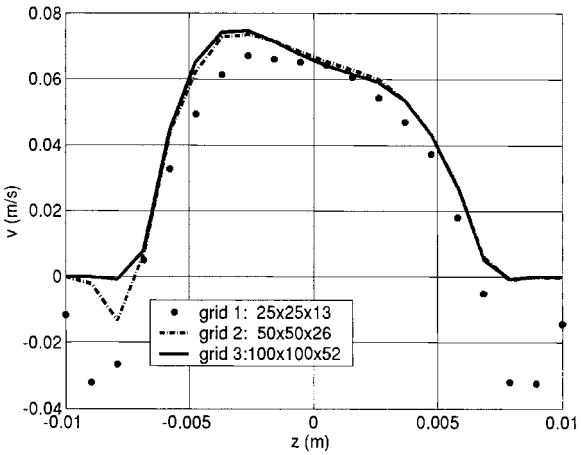

Figure 6. Axial velocity profile on a vertical line segment at the end of the bend.

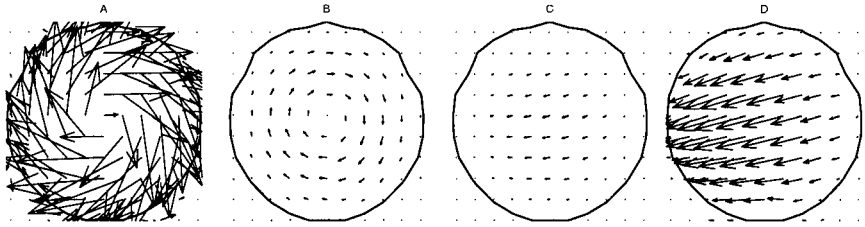

Figure 7. Re = 1: Inflow area at several x-values; A,B,C,D (see Figure 5).

$$h_{\text{axis}} = 0{\cdot}012\ \cos(\theta + \frac{3}{2}\pi)$$

where θ decreases from $\frac{\pi}{2}$ at the end of the entrance down to $-\pi$ at the beginning of the outlet.

Several grid refinement studies were performed. In Figure 6, the velocity profile, in this case for Re = 100, after two seconds is shown on a line segment at the end of the helical part. The maximum velocity is clearly at the lower part of the tube. Note the large differences on the left and on the right; they are caused by interpolation of mirror velocities outside the wall; these mirror velocities can become quite high, depending on the positions where the boundary cuts the cells, but they do not influence computations of secondary quantities like the wall shear stress (see above). A computational grid of $50 \times 50 \times 26$ proved to be adequate enough for our purposes.

The cross-sectional areas, where the secondary velocities are shown, (see below) are depicted in Figure 5.

We would like to answer the following questions:

– How long will secondary velocities, once formed, persist?

– Will the strong curvature induce secondary velocities, and if so, to which extent?

3.2. Secondary velocities in the inlet

We start with an investigation of the effect of initial disturbances. The inflow velocity is described by a parabolic profile in the axial direction combined with a single vortex in the cross-sectional area. In this way we are simulating the spiraling flow as presented by Bremer (see Section 1).

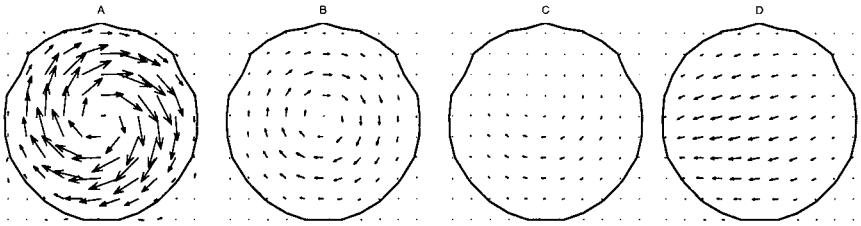

Figure 8. Re = 10: Inflow area at several x-values: A,B,C,D.

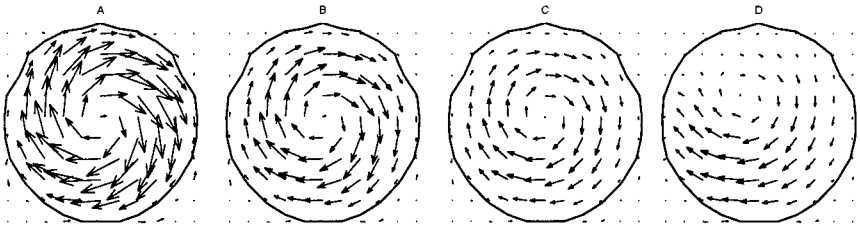

Figure 9. Re = 100: Inflow area at several x-values: A,B,C,D; note: arrows are enlarged by a factor of 5.

The mathematical description of the velocity $\boldsymbol{u}$ at the entrance is

$$u(y,z) = U(1 - \frac{r^2}{R^2}),$$

$$v(y,z) = U(1 - \frac{r^2}{R^2})(z - z_c),$$

$$w(y,z) = -U(1 - \frac{r^2}{R^2})(y - y_c),$$

where (y_c, z_c) is the centre of the circular cross-section; the distance of (y, z) to the centre is given by $r = \sqrt{(y - y_c)^2 + (z - z_c)^2}$.

The magnitude of the secondary velocities is 38% of the axial velocity. Quiver plots at cross-sections downstream show that these initial secondary patterns fade away rather quickly, mainly because of the very low Reynolds number (see Figures 7 and 5 for the locations of the cross-sections). If we repeat the simulation with the inlet velocities (and therefore the Reynolds number) multiplied by factors 10 and 100, we get the results shown in Figures 8 and 9. Note the irregular shape of the geometry while one would expect a purely circular shape. The explanation is that the drawn line is a reconstructed isoline of the geometry aperture F_b at level 0·5. The velocities in the plots are all on the same scale for Re = 100 and Re = 10; however, for viewing purposes the velocities in the Re = 1 plots are enlarged by an extra factor 5.

The strength of the vortices decays so rapidly that, especially for lower Reynolds numbers the velocities already start to follow the entrance of the first bend; the lower the Reynolds number, the further upstream this will occur. It is only in the Re = 100 case that the secondary flow field can maintain itself until it reaches the bend.

To summarize this effect, the strength of the secondary flow field, defined as the overall maximum of the two non-axial velocity components, was computed for the three cases (Figure 10). The x-axis represents the whole straight inlet, from A (left) to D (right). Note that the influence of the beginning of the helical part is already visible on the right, where the magnitude of the secondary velocities increases again.

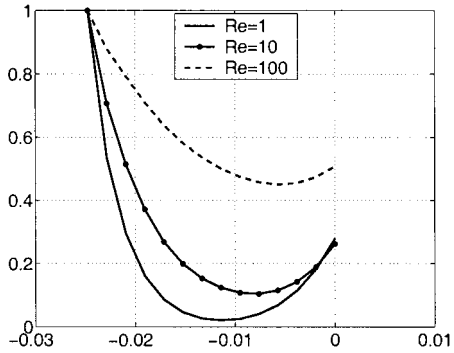

Figure 10. Relative decay of the strength of the vortex in the inlet, from A ($x = -0{\cdot}024$) to D ($x = 0$).

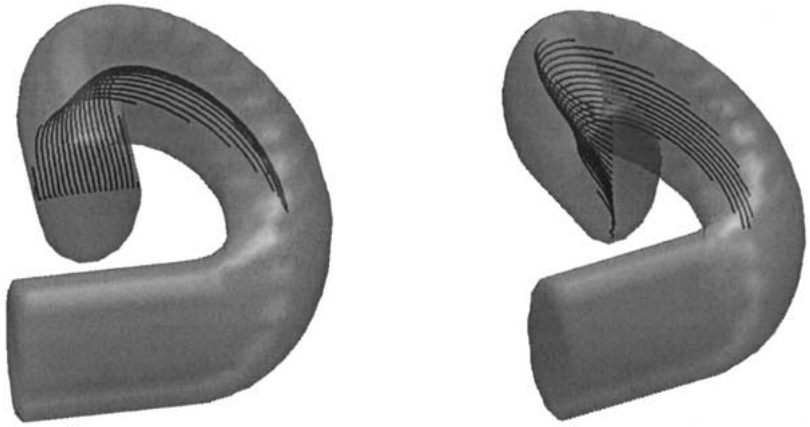

Figure 11. Streamlines of particles released from a horizontal line (left) and a vertical line (right) at the inlet (Re = 10).

We also calculated the streamlines starting in two perpendicular planes for the same simulation. This is done by setting several (in this case 20) massless particles uniformly distributed on a line segment. Each time cycle the positions of the particles are updated by integration in time; velocities needed at those positions are obtained by linear interpolation of the eight discrete velocities around them. Figure 11 displays a view for each of them, for Re = 10. It is clear that, after the initial, forced rotation, the streamlines follow a 'parallel' pathway, again demonstrating the limited influence of the secondary velocities. Note also that the parabolic character of the axial velocity leads to the much shorter streamlines of particles starting close to the wall. Obviously, the strong curvature of the tube does not generate secondary velocities, as the experimental result of Bremer (Figure 1) already suggested.

Finally, Figure 12 shows a comparison of the effects, on particles starting on the horizontal line, of the three different Reynolds numbers.

3.3. INFLUENCE OF THE HELIX ON THE OUTLET

Now we return to standard Poiseuille flow at the inlet, so as to be sure that the velocity field at the beginning of the bend is the same for all Reynolds numbers. Theoretically it is well known that in a tube that is curved in one plane, say the x, y-plane, a typical secondary velocity field will form, consisting of two vortices separated by the $z = 0$ plane. The intuitive explanation

Figure 12. Streamlines starting on a horizontal plane, for Re = 1 (left), Re = 10 (middle) and Re = 100 (right).

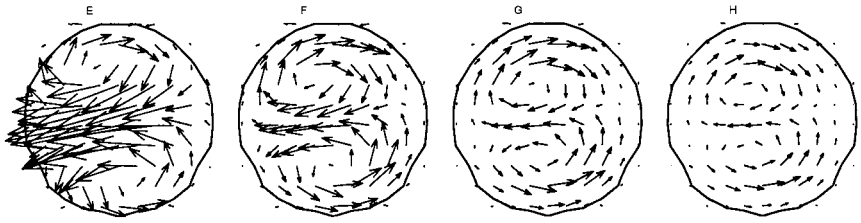

Figure 13. Re = 100: Straight part after the bend; cross sections at E,F,G,H.

is the following: particles traveling along the bend are subjected to a lateral force mv^2/R, where R is the radius of curvature, v the axial velocity and m the mass. This force has to be provided by the pressure gradient. This pressure gradient is approximately uniform. The velocity v, however, depends on the distance of a particle from the wall: near the wall, this velocity approaches zero. Thus the velocity of the particles in the core is too large, making them sweep towards the outer bend, while the particles near the wall slowly move towards the inner bend (see Figure 14).

In our case, since the helix is not curved in one plane, the separation line between the vortices is not horizontal but has an angle. This can be seen in the quiver plots in the planes at the beginning of the straight part (E). Additional quiver plots are shown at positions further downstream; see again Figure 5 for the locations.

The lengths of the arrows of plots having the same Reynolds number are on the same scale. However, velocity arrows of the Re = 10 case are additionally enlarged by a factor of 4 compared to the Re = 100 case; this extra factor is 50 for the Re = 1 plots.

At Re = 100, the secondary velocity pattern persists up to the outflow area (see Figure 13). The angle of the two vortices with the (x, y)-plane begins to vanish.

At the more realistic Reynolds numbers of 10 and 1 (Figures 15 and 16) the effect is much smaller. Note the irregularities in plots H and I of the Re = 10 case: however, these are merely small perturbations since the magnitude of these secondary velocities about 0·8% of the magnitude of the axial velocity. The plots for Re = 1 show the same phenomenon: a quick diminishing of the secondary velocities, and same irregularities, *i.e.*, very small cross-sectional patterns that most probably originate from discretization errors; in any case, their strength is less than half a percent of the main flow.

So it is clear that the influence of the bend is very short-lived in the Re = 1 case; only at higher Reynolds number, a more considerable effect is seen to persist downstream.

It is interesting to see how the secondary velocities cause a non-uniform wall shear stress, since it is generally thought that areas with wall-shear-stress values outside certain ranges can induce morphological changes. As could be expected from the results above, the wall shear

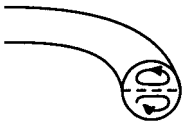

Figure 14. Vortex structure in a curved tube.

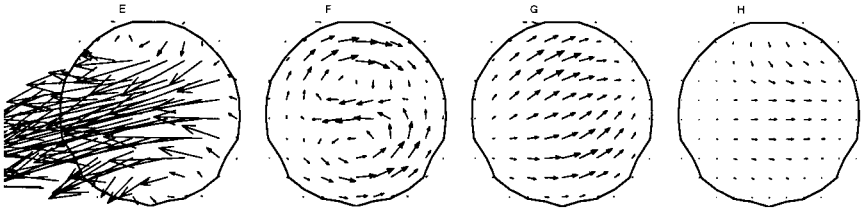

Figure 15. Re = 10: Straight part after the bend; cross-sections at E,F,G,H; note: arrows are enlarged by a factor of 4.

stress (WSS) in the straight parts in the Re = 1 case is mostly uniform (see Figure 17). The geometry is viewed from below. Thus, after a curve of 270 degrees, the WSS pattern almost immediately returns to the standard uniform pattern for Poiseuille flow, where $\mathrm{WSS} = \mu 2U/R$ everywhere. In the right subplot of Figure 17 the differences in the distribution are greater and an axisymmetric pattern of the WSS does not return, at least not before the outflow area.

The irregular spots of different grey values are artefacts caused by the mapping of the geometry on the Cartesian grid. However, in both cases, the WSS in the helical part of the geometry is significantly higher on the inner bend and lower on the outer bend, which is a typical effect in flows with low Dean numbers.

4. Discussion

In this first assessment of the possible influence of hemodynamic forces on the morphogenesis of the heart we have studied a geometrically simple model with realistic dimensions. Because it has been suggested in literature that the wall shear stress is an intermediate step in the interaction between blood flow and surrounding tissues, we studied the spatial distribution of the wall shear stress under various conditions in search for heterogeneity of the distribution of the wall shear stress according to a pattern that would seem reasonable in view of the subsequent morphogenic events. From the results it has become clear that, within the bend, the WSS shows heterogeneity, but a spiraling pattern was not found. One might argue that, in the subsequent stages of the development, the Reynolds number will increase rapidly. Therefore, we have studied the same geometry at the Reynolds number of 100 and regain observed a very small secondary flow pattern and a limited heterogeneity of the wall shear stress. Against the background that a Reynolds number of 100 will only be reached in the developmental stage when the spiraling septum in the outflow tract is completed, we must conclude that, within the limitations of the model, no biologically meaningful pattern of the wall shear stress will occur during the development. Moreover, the spiraling pattern in the inlet, as observed by Bremer [16] decays very rapidly and does not influence the flow pattern or the WSS in the outflow. This study supports the conclusion of Seidl and Steding [17] that the changing morphology precedes and induces the spiraling flow pattern.

Two factors have not yet been included in the present model: the pulsatility of the flow and the movement of the wall of the developing heart. The influence of the pulsatility can be

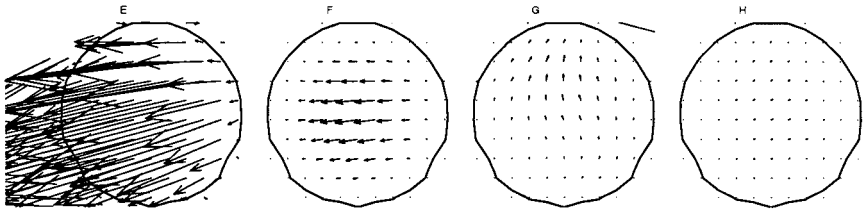

Figure 16. Re = 1: Straight part after the bend; cross-sections at E,F,G,H; note: arrows are enlarged by a factor of 50.

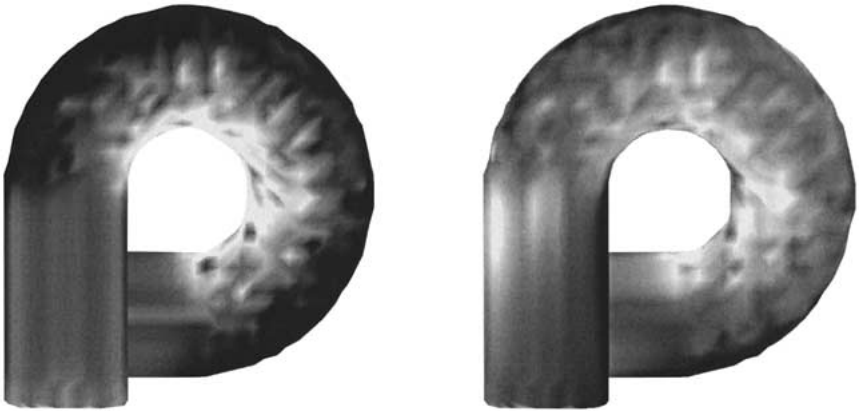

Figure 17. WSS patterns, Re = 1 (left), Re = 100 (right).

estimated on the basis of the Womersley number, $r\sqrt{\omega\rho/\mu}$, where r is the radius, ω the frequency, ρ the density and μ the dynamic viscosity. Like the other dimensionless parameters, the Womersley number is very small due to the small diameter of the tube, and consequently no major distortion of the flow patterns due to pulsatility is to be expected.

The influence of the movement of the wall is difficult to assess. This may be a factor in creating the heterogeneity of the wall shear stress. The only thing that can be said now is that in early stages the amplitude of these movements is less than 10% of the diameter of the tube, but a definite statement can only be made once the movement has been recorded accurately in time and space and is added to the model.

Meanwhile, however, the present model of ComFlo has been extended, resulting in simulations with moving elastic walls that have been performed for a model of the basilar artery [22]; therefore, the present investigation on the embryonal heart will be continued.

References

1. B. Hogers, *The Role of Blood Flow in Normal and Abnormal Heart Development.* Ph.D thesis, Rijksuniversiteit Leiden (1998) 146pp.
2. P.F. Davies, Flow-mediated endothelial mechanotransduction. *Physiol. Rev.* 75 (1995) 519–560.
3. O. Traub and B.C. Berk, Laminar shear stress. Mechanisms by which endothelial cells transduce an atheroprotective force. *Arterioscler. Thromb. Vasc. Biol.* 18 (1998) 677–685.
4. S. Chien, S. Li and Y.J. Shyy, Effects of mechanical forces on signal transduction and gene expression in endothelial cells. *Hypertension* 31, part 2 (1998) 162–169.
5. W.R. Dean, Note on the motion of a fluid in a curved pipe. *Philos. Mag.* 4 (1927) 208–233.
6. D.J. McConalogue and R.S. Srivastava, Motion of fluid in a curved tube. *Proc. R. Soc. London A* 307 (1968) 37–53.

7. D.J. McConalogue, The effects of secondary flow on the laminar dispersion of an injected substance in a curved tube. *Proc. R. Soc. London A* 31 (1970) 99–113.
8. W.H. Lyne, Unsteady viscous flow in a curved pipe. *J. Fluid Mech.* 45 (1970) 13–31.
9. L.R. Austin and J.D. Seader, Fully developed viscous flow in coiled circular pipes. *AIChE J.* 19 (1973) 85–94.
10. R.G. Zalosh and W.G. Nelson, Pulsating flow and a curved tube. *J. Fluid Mech.* 59 (1973) 693–705.
11. J.M. Tarbell and M.R. Samuels, momentum and heat transfer in helical coils. *Chem. Eng. J.* 5 (1973) 117–127.
12. R.J. Nunge and T.S. Lin, Laminar flow in strongly curved tubes. *AIChE J.* 19 (1973) 1280–1281.
13. J.Y. Lin and J.M. Tarbell, Periodic flow in a curved tube. *AIChE J.* 26 (1980) 165–168.
14. J. Kaczinsky, J.W. Smith and R.L. Hummel, Laminar flow in the central plane of a curved circular pipe. *Can. J. Chem. Engng.* 33 (1975) 221–224.
15. Y. Agrawal, L. Talbot and K. Gong, Laser anemometer study of flow development in curved circular pipes. *J. Fluid Mech.* 85 (1978) 497–518.
16. J.L. Bremer, The presence and influence of two spiral streams in the heart of the chick embryo. *Am. J. Anat.* 49 (1932) 409–440.
17. W. Seidl and G. Steding, Die Bedeutung der Herzwand für die Gestaltung des Blutstroms. *Verh. Anat. Ges.* 80 (1987) 47–49.
18. G. Yang, D.M. Causon and D.M. Ingram, Calculation of compressible flows about complex moving geometries using a 3d Cartesian cut cell method. *Int. J. Num. Meth. Fluids* 33 (2000) 1121–1151.
19. D.M. Causon, D.M. Ingram, C.M. Mingham, G. Yang and R.V. Pearson, Calculation of shallow water flows using a Cartesian cut cell approach. *Adv. Water Resources* 23 (2000), 545–562.
20. J. Gerrits, *Dynamics of Fluid-Filled Spacecraft.* Ph.D thesis, Rijksuniversiteit Groningen (2001) 112pp.
21. R.W.C.P. Verstappen and A.E.P. Veldman, Spectro-consistent discretization: a challenge to RANS and LES. *J. Engng. Math.* 34 (1998) 163–179.
22. G.E. Loots, B. Hillen, H.W. Hoogstraten and A.E.P. Veldman, Fluid-structure interaction in the basilar artery. *J. Engng. Math.*, to be published (2003).